Transactions on Machine Intelligence 2(4) (2019) 221-234

ISSN Online: 2821-1693

Transactions on Machine Intelligence

Journal Homepage: https://tmachineintelligence.ir/index.php/TMI

Brain Tumor Segmentation in MRI Images Using Transform Domain Methods

A. AshamiPour[1], H. Yarahmadi[2,*], J. Mohammadzadeh[2]

[1] Department of Computer Science, Buin Zahra Branch, Islamic Azad University, Buin Zahra, Iran
[2] Assistant Professor, Department of Computer Science, Buin Zahra Branch, Islamic Azad University, Buin Zahra, Iran

ARTICLE INFO

Article History:
Received 4 August 2019
Received in revised form 26 October 2019
Accepted 16 December 2019
Available online 19 December 2019

Keywords:
Segmentation, MRI Image, Contourlet, Brain Tumor

ABSTRACT

Image segmentation techniques are widely used in medical imaging to isolate homogeneous regions. To date, no complete image segmentation method has been presented that can yield satisfactory results for imaging applications such as brain MRI, brain cancer detection, and others. This study presents a method for brain tumor segmentation in MRI images using transform domain methods and contourlets. First, a multi-resolution representation of the input image is created using the contourlet transform. Then, an 8-dimensional feature vector is extracted for each pixel using inter-resolution and intra-resolution data. The final feature vector's dimensions are reduced using Principal Component Analysis (PCA). Finally, the feature vectors are grouped into discrete clusters for segmentation. The proposed method was implemented on brain images using MATLAB software. The algorithm is computationally simple, yet efficient for brain tumor segmentation in MRI images. Using the eight subbands, as opposed to the conventional wavelet transform that extracts coefficients in only three directions, helps us better identify directional details in the image. Additionally, the use of eight directional features for each pixel allows the extracted details in different subbands to be enhanced in accordance with the direction, making maximal use of the subband correlation. The proposed method does not suffer from the region overlapping problem of active contour methods and can detect the internal areas of large regions. Overall, the proposed algorithm improves performance by six percent compared to the active contour method and by one percent compared to the two-dimensional feature extraction method using wavelet transform.

1. INTRODUCTION

Segmentation is a critical process in medical image analysis that involves partitioning an image into meaningful regions or components. It plays a vital role in identifying and delineating areas of interest, such as tumors, organs, or other anatomical structures, which is essential for accurate diagnosis and treatment planning. The advent of deep learning, particularly Convolutional Neural Networks (CNNs), has revolutionized the approaches to segmentation in medical imaging, enhancing the accuracy and efficiency of these processes [1-6].

---

[*] Corresponding Author: hsyara@gmail.com
Assistant Professor, Department of Computer Science, Buin Zahra Branch, Islamic Azad University, Buin Zahra, Iran

http://dx.doi.org/10.47176/TMI.2019.221

Segmentation divides an image into regions of components or objects and is a crucial tool in medical image processing [7]. By identifying all the pixels (in a 2D image) or voxels (in a 3D image) belonging to an object, segmentation isolates a specific object [8]. In medical imaging, segmentation is vital for feature extraction, image measurement, and image visualization [9]. Brain structure segmentation in magnetic resonance imaging (MRI) holds the highest significance, which distinguishes MRI from other methods and makes it suitable for volumetric analysis of brain tissues, such as multiple sclerosis (MS), schizophrenia, epilepsy, Parkinson's disease, Alzheimer's disease, brain atrophy, and others [10]. In image segmentation, the degree to which an image is divided into its constituent regions or objects depends on the problem to be solved. In other words, segmentation should stop when the target of interest is separated. The main objective of segmentation is to divide the image into parts that have a strong correlation with the regions of interest in the image. Segmentation can primarily be classified as either complete or partial. The results of complete segmentation correspond only to discrete regions of the input image, whereas the regions resulting from partial segmentation are not directly related to the input image [11].

In medical imaging, segmentation is used to analyze anatomical structures such as bones, muscles, blood vessels, various tissues, pathological regions such as cancer, multiple sclerosis lesions, and to divide a full image into sub-regions such as white matter (WM), gray matter (GM), and cerebrospinal fluid (CSF) in automatic brain mapping [8]. In the domain of medical image processing, brain MRI segmentation is of particular importance because MRI, specifically due to its excellent contrast of soft tissues, non-invasive nature, and high spatial resolution, is well-suited for brain studies. Image segmentation is an essential tool in medical image processing and is used in various applications. For example, in medical imaging, it is used for the detection of multiple sclerosis lesions, surgical planning, simulated surgeries, tumor localization, other pathologies, tissue volume measurement, brain MRI segmentation, anatomical structure studies, and more [9]. In June 2016, Saha and colleagues performed brain image segmentation using semi-supervised clustering. This technique was implemented using multi-objective optimization concepts in the intensity space. This method also utilizes three clustering validity indices as the objective function, which are simultaneously optimized using AMOSA [12].

In another study by Jiang et al. in 2013, a method was proposed to construct a graph using a set of population learning features and patient-specific features in MRI images, which ultimately uses graph cuts to achieve the final segmentation. The performance of the proposed method was evaluated using 23 glioma image sequences and compared with some established methods [13]. In a further study conducted by Vasileios et al. in 2015, a cost-effective, unsupervised combined algorithm was proposed. In this approach, to extract local and global information from brain tissues and model imaging profiles in both healthy and malignant conditions, four common MRI sequences T1-weighted, T1 gadolinium-enhanced, T2-weighted, and inverse fluid attenuation recovery are combined with machine learning techniques. The results of this study show that the proposed method achieves accuracy similar to current methods, with lower computational cost and a higher degree of automation [14].

2. MATERIALS AND METHODS

2.1. Introduction to the Level Set Method with Distance Regularization

This study proposes a more general formulation for variable surface regularization in the form of a distance regularization term and an external energy term, which guides the movement of the zero-level contour to the desired position. In surface evolution, the level set function (LSF) is maintained through the fast marching method (FAB) derived from the distance regularization term. As a result, the distance regularization eliminates the need for re-initialization in a systematic method, avoiding the undesirable effects introduced by the error term in the initial work [15], thus the surface evolution is called the Distance-Regularized Level Set Evolution (DRLSE) formulation.

2.2. DRLSE

In level set methods, a contour is embedded as the zero-level of the LSF. Although the final result of the level set method is the zero-level of the LSF, it is necessary to maintain the LSF in a good condition so that the surface evolution remains stable and numerical computations are accurate. This requires that the LSF be smooth during surface evolution, neither too fast nor too flat. These conditions are satisfied by the signed distance functions due to their unique characteristic $|\nabla\phi|=1$, which refers to the signed distance property. For example, in the two-dimensional case, consider the signed distance function $z=\phi(x,y)$ as a surface. Then its tangent plane forms a 45-degree angle with both the xy-plane and the axis, which can be easily verified by the signed distance property $|\nabla\phi|=1$. For this desirable property, signed distance functions are widely used as level set functions in level set methods. In the conventional level set formulation, the LSF is usually initialized and periodically re-initialized as a signed distance function. This section presents a level set formulation that inherently preserves this desirable property of the LSF.

2.2.1. Energy Formulation with Distance Regularization

Let $\phi: \Omega \to \Re$ define the level set function (LSF) in the domain Ω. The energy function $\varepsilon(\phi)$ is defined as follows:

$$\mathscr{E}(\phi) = \mu\mathcal{R}_p(\phi) + \mathcal{E}_{ext}(\phi) \tag{1}$$

where $\mathcal{R}_p(\phi)$ is the level set regularization term, $\mu > 0$ is a constant, and $\mathcal{E}_{ext}(\phi)$ is the external energy term, which depends on the relevant information (i.e., the image for image segmentation applications). The level set regularization term $\mathcal{R}_p(\phi)$ is defined as follows:

$$\mathcal{R}_p(\phi) \triangleq \int_\Omega p(|\nabla\phi|)dx \tag{2}$$

where p is the potential function (or energy density), defined as $p: [0,\infty) \to \Re$. The energy $\mathcal{E}_{ext}(\phi)$ is designed so that it reaches its minimum when the zero level set LSF(ϕ) is positioned at the desired location. Minimizing the energy $\mathcal{E}(\phi)$ can be achieved by solving the level set evolution equation, which is presented in the next section.

A simple choice for the potential function in the regularization term $\mathcal{R}_p$ is $p(s) = s^2$, which forces $|\nabla\phi|$ to be zero. Such a level set regularization term has a strong smoothing effect, but it also flattens the LSF, ultimately causing the zero level set contour to disappear.

In fact, the goal of applying the level set regularization term is not only to smooth LSF(ϕ) but also to preserve the signed distance property $|\nabla\phi| = 1$, at least in the vicinity of the zero level set, to ensure accurate computations for curve evolution. This goal can be achieved by using a potential function $p(s)$ that has a minimum at $s = 1$, so that the level set regularization term $\mathcal{R}_p(\phi)$ reaches its minimum when $|\nabla\phi| = 1$. Therefore, the potential function $p(s)$ should have a minimum at $s = 1$ (although it may have other minima as well).

The potential function p is used in the proposed variational level set formulation (Equation 1). The corresponding level set regularization term $\mathcal{R}_p(\phi)$ refers to the distance regularization term for its role in preserving the signed distance property of the LSF. A proper and simple definition of the potential function ppp for distance regularization is given as follows:

$$p = p_1(s) \triangleq \frac{1}{2}(s-1)^2 \tag{3}$$

where $s = 1$ is the unique minimum point. With the potential function $p = p_1(s)$, the distance regularization term $\mathcal{R}_p(\phi)$ can be expressed more simply as follows:

$$\mathcal{P}(\phi) = \frac{1}{2}\int_\Omega(|\nabla\phi| - 1)^2dx \tag{4}$$

where the derivative of ϕ is determined by the signed distance function. The energy function $\mathcal{P}(\phi)$, acting as an error term, is proposed to maintain the signed distance property throughout the entire domain. However, the level set evolution derived to minimize the energy has an undesirable side effect on LSF(ϕ) in certain situations.

To avoid this side effect, a new potential function p is introduced in the distance regularization term $\mathcal{R}_p$. This new potential function aims to preserve the property $|\nabla\phi| = 1$ only in the vicinity of the zero level set, while keeping LSF constant with $|\nabla\phi| = 0$ in regions far from the zero level set.

To maintain such an LSF profile, the potential function $\mathrm{p(s)}$ must have minimum points at $\mathrm{s} = 1$ and $\mathrm{s} = 0$. This type of potential function is known as a double-well potential, meaning it has two minima. The double-well potential $\mathrm{p} = \mathrm{p}_2$ is clear and well-defined. By using the double-well potential $\mathrm{p} = \mathrm{p}_2$, not only is the side effect occurring with $\mathrm{p} = \mathrm{p}_1$ avoided, but it also introduces certain numerically and theoretically appealing properties in level set evolution.

2.2.2. Gradient Flow for Energy Minimization

In unstable algebra [16], a standard approach for minimizing the energy function $\mathscr{F}(\phi)$ is to find a stable solution to the gradient flow equation:

$$\frac{\partial \phi}{\partial \mathrm{t}} = -\frac{\partial \mathscr{F}}{\partial \phi} \tag{5}$$

where $\frac{\partial \mathscr{F}}{\partial \phi}$ represents the Gâteaux derivative of the function $\mathscr{F}(\phi)$. This equation describes an evolutionary process for the time-independent function $\phi(\mathrm{x}, \mathrm{t})$, where x is the spatial variable in the domain Ω and $\mathrm{t} \geq 0$ is the temporal variable. The evolution begins with the initial function $\phi(\mathrm{x}, 0) = \phi_0(\mathrm{x})$.

The time evolution of the function $\phi(\mathrm{x}, \mathrm{t})$ follows the negative direction of the Gâteaux derivative, i.e., $-\partial \mathcal{F} / \partial \phi$, which corresponds to the steepest descent direction of the function $\mathscr{F}(\phi)$. Consequently, this gradient flow is also referred to as the steepest gradient descent flow or simply the gradient descent flow.

The Gâteaux derivative of the function $\mathcal{R}_{\mathrm{p}}(\phi)$ in equation (2) is given by:

$$\frac{\partial \mathcal{R}_{\mathrm{p}}}{\partial \phi} = -\mathrm{div}\big(\mathrm{d}_{\mathrm{p}}(|\nabla \phi|) \nabla \phi\big) \tag{6}$$

where $\mathrm{div}(0)$ is the divergence operator, and d_{p} is a function defined as follows:

$$\mathrm{d}_{\mathrm{p}}(\mathrm{s}) \triangleq \frac{\mathrm{p}'(\mathrm{s})}{\mathrm{s}} \tag{7}$$

From equation (1) and the linearity of the Gâteaux derivative, we have:

$$\frac{\partial \mathcal{E}}{\partial \phi} = \mu \frac{\partial \mathcal{R}_{\mathrm{p}}}{\partial \phi} + \frac{\partial \mathcal{E}_{\mathrm{ext}}}{\partial \phi} \tag{8}$$

Where $\frac{\partial \mathcal{E}_{\mathrm{ext}}}{\partial \phi}$ is the Gâteaux derivative of the external energy function $\mathcal{E}_{\mathrm{ext}}$ with respect to ϕ. Then, the gradient flow of the energy $\mathcal{E}(\phi)$ is as follows:

$$\frac{\partial \phi}{\partial \mathrm{t}} = -\mu \frac{\partial \mathcal{R}_{\mathrm{p}}}{\partial \phi} - \frac{\partial \mathcal{E}_{\mathrm{ext}}}{\partial \phi} \tag{9}$$

When combined with equation (6), it can be expressed as follows:

$$\frac{\partial \phi}{\partial \mathrm{t}} = \mu \mathrm{div}\big(\mathrm{d}_{\mathrm{p}}(|\nabla \phi|) \nabla \phi\big) - \frac{\partial \mathcal{E}_{\mathrm{ext}}}{\partial \phi} \tag{10}$$

This PDE is the level-set evolution equation derived from the proposed variable formulation in equation (1). We solve this PDE with Neumann boundary conditions [17] and the initial function ϕ_0. The level-set evolution in equation (10) DRLSE is invoked with the inherent ability to preserve the signed distance property of LSF, which is related to the distance regularization term $\mathcal{R}_{\mathrm{P}}$ in equation (1). Re-initialization in the DRLSE implementation is not required due to the intrinsic distance regularization effect embedded in the level-set evolution. The level-set evolution without re-initialization in the initial work [15] is a special case of DRLSE in equation (10). The effect of the distance regularization in DRLSE can be observed from the gradient flow of the energy term $\mu\mathcal{R}_P(\phi)$.

$$\frac{\partial\phi}{\partial t} = \mu\mathrm{div}(d_p(|\nabla\phi|)\nabla\phi \tag{11}$$

This flow can be expressed in a standard form of the diffusion equation with a diffusion rate $D = \mu d_p(|\nabla\phi|)$;

$$\frac{\partial\phi}{\partial t} = \mathrm{div}(D\nabla\phi)$$

Therefore, the flow in equations (10) and (11) exhibits a diffusion effect in the level set function ϕ. This diffusion is not ordinary, as the diffusion rate $\mu d_p(|\nabla\phi|$ can be either positive or negative for the potential pp used in DRLSE. When $d_p(|\nabla\phi|$ is positive, the diffusion is forward, causing $|\nabla\phi|$ to decrease. When $d_p(|\nabla\phi|$ is negative, the diffusion is backward, causing $|\nabla\phi|$ to increase. Such diffusion is called FAB diffusion. This FAB adaptively increases or decreases $|\nabla\phi|$ to ensure it is forced to approach the minima of the potential function $p(s)$, thereby preserving the desired shape of the function ϕ\phi. For the potential $p = p_1$ defined in equation (3), we have $d_p(s) = 1 - (1/s)$. In this case, the PDE in equation (10) can be expressed as follows:

$$\frac{\partial\phi}{\partial t} = \mu\left[\nabla^2\phi - \mathrm{div}\left(\frac{\nabla\phi}{|\nabla\phi|}\right)\right] - \frac{\partial\mathcal{E}_{\mathrm{ext}}}{\partial\phi} \tag{12}$$

The operator ∇^2 is the Laplacian operator. It is important to note that the expression div $\left(\frac{\nabla\phi}{|\nabla\phi|}\right)$ calculates the mean curvature of the level set contours of the function ϕ. The sign of the function $d_p(s) = 1 - (1/s)$، indicates the characteristic of the FAB diffusion expression in the following two cases:

- For $|\nabla\phi|>1$, the diffusion rate $\mu d_p(|\nabla\phi|)$ is positive, and the diffusion in equation (11) is forward, causing $|\nabla\phi|$ to decrease.
- For $|\nabla\phi|<1$, the diffusion rate $\mu d_p(|\nabla\phi|)$ is negative, and the diffusion is backward, causing $|\nabla\phi|$ to increase.

Thus, the FAB diffusion with the potential $p = p_1$ forces $|\nabla\phi|$ to have a value of 1 to preserve the sign distance characteristic. However, this FAB diffusion has an infinite diffusion rate $\mu d_p(|\nabla\phi|) = \mu(1 - 1/|\nabla\phi|))$, which tends to zero as $|\nabla\phi|$ approaches infinity. This can lead to an undesirable side effect in LSFϕ when $|\nabla\phi|$ is near zero. This side effect can be avoided by using the double-well potential, i.e., $p = p_2$, where the diffusion rate $\mu d_p(|\nabla\phi|)$ is limited by a constant.

2.2.3. Double-Well Potential for Distance Regularization

The preferred potential function p for the distance regularization term $\mathscr{R}_p$ is the double-well potential. Here, a specific structure of the double-well potential, $p_2(s)$, is presented:

$$p_2(s) = \begin{cases} \frac{1}{(2\pi)^2}(1 - \cos(2\pi s)), & \text{if } s \le 1 \\ \frac{1}{2}(s-1)^2, & \text{if } s \ge 1 \end{cases} \tag{13}$$

This potential $p_2(s)$ has two minima at $s = 0$ and $s = 1$. To verify that p_2 is twice differentiable over the interval $[0, \infty)$, we compute its first and second derivatives as follows:

$$p_2'(s) = \begin{cases} \frac{1}{2\pi}\sin(2\pi s), & \text{if } s \le 1 \\ s - 1 & \text{if } s \ge 1 \end{cases}$$

and

$$p_2''(s) = \begin{cases} \cos(2\pi s), & \text{if } s \le 1 \\ 1 & \text{if } s \ge 1 \end{cases}$$

The function $p_2(s)$, its derivatives $p_2'(s)$ and $p_2''(s)$. It is easily verified that the function $d_p(s) = p_2'(s)/s$ satisfies the following conditions:

$$|d_p(s)| < 1, \quad \text{for all } s \in (0, \infty) \tag{14}$$

and

$$\lim_{s\to 0} d_p(s) = \lim_{s\to\infty} d_p(s) = 1 \tag{15}$$

So we have;

$$|\mu d_p(|\nabla\phi|) \le \mu$$

2.2.4. Effect of Distance Regularization

We demonstrate the effect of DRLSE distance regularization through the simulation of FAB diffusion in equation (11), using the initial function ϕ_0, which is a binary step function. The binary step function ϕ_0 is defined as follows:

$$\phi_0(x) = \begin{cases} -c_0 & \text{if } x \in R_0 \\ c_0 & \text{otherwise} \end{cases} \tag{16}$$

where $c_0 > 0$ is a constant and R_0 is a region in the domain. Despite the irregularity of the binary step function, the FAB diffusion in equation (11) is capable of evolving the LSF into a well-ordered function. The effect of distance regularization with the double-well potential, $p = p_2(s)$, can be observed from the numerical simulation of FAB diffusion in equation (11). We use the binary step function $\phi_0$on a 100×100 grid, as defined by equation (16), with the rectangular region R_0.

2.2.5. Finite Difference Scheme

The DRLSE in (10) can be implemented using a simple finite difference scheme. We consider the two-dimensional case with the time-independent LSF$\phi(x, y, t)$. The spatial derivatives $\phi\,\partial/\,\partial x$ and $\phi\,\partial/\,\partial x$ in our model are approximated using central differences. A fixed spatial step $\Delta x = \Delta y = 1$ is used to compute the spatial derivatives. The time derivative $\phi\,\partial/\,\partial t$ is approximated using a forward difference. The time-independent LSF$\phi(x, y, t)$ is discretized in the form $\phi_{i,j}^k$, with the spatial index (i,j) and the time index kk. Thus, the level set evolution equation, analogous to the finite difference equation $(\phi_{i,j}^{k+1} - \phi_{i,j}^k)/\Delta t = L(\phi_{i,j}^k)$, is discrete, where $L(\phi_{i,j}^k)$ approximates the right-hand side of the evolution equations. These equations can be expressed as follows:

$$\phi_{i,j}^{k+1} = \phi_{i,j}^k + \Delta t L(\phi_{i,j}^k), \quad k = 0,1,2,\ldots \tag{17}$$

In the numerical implementation of DRLSE, the iterative process is used. Assuming a spatial step $\Delta x = \Delta y = 1$, the time step for this finite difference scheme must satisfy the CFL condition, i.e., $\mu\Delta t < (1/4)$, for numerical stability. In practice, a relatively large time step $\Delta t > 1$ can be used to accelerate the curve evolution, while the parameter μ\mu should be relatively small to meet the CFL condition.

It is worth noting that although the FAB diffusion term in DRLSE arises from the proposed variable level set formulation in (1), it can be incorporated into more general level set evolution equations that do not necessarily result from the variable formulation. For instance, consider the evolution equation of a conventional level set formulation:

$$\frac{\partial \phi}{\partial t} = F|\nabla \phi| + A.\nabla \phi \tag{18}$$

Where F is a scalar function and A is a vector magnitude function. In the standard numerical solution for this PDE, the spatial derivatives are discretized using the Upwind scheme [18]. The central difference scheme for this PDE is not stable. By adding the distance regularization term to the PDE, the level set equation in 18 becomes a DRLSE formulation.

$$\frac{\partial \phi}{\partial t} = \mu \mathrm{div}\big(d_p(|\nabla \phi|)\nabla \phi\big) + F|\nabla \phi| + A.\nabla \phi \tag{19}$$

By adding the distance regularization term, all spatial derivatives in equation (19) can be discretized using the central difference scheme. The corresponding numerical scheme is stable without the need for re-initialization. It is evident that the central difference scheme is more accurate and efficient than the first-order upwind scheme, which is typically used in conventional level set formulations.

2.3. Application in Image Segmentation

2.3.1. Edge-Based Active Contour Model in Distance Regularized Level Set Formulation

Let I be an image in domain Ω, and now we define the edge indicator function g as follows:

$$g \triangleq \frac{1}{1+|\nabla G_\sigma * 1|^2} \tag{20}$$

where G_σ is the Gaussian kernel with standard deviation σ. The convolution in equation (20) is used for image smoothing in order to reduce noise. This function g typically takes smaller values at the boundaries of the object compared to other regions. For LSF$\phi: \Omega \to \Re$, the energy function $\mathcal{E}(\phi)$is defined as follows:

$$\mathcal{E}(\phi) = \mu \mathcal{R}_p(\phi) + \lambda \mathcal{L}_g(\phi) + \alpha \mathcal{A}_g(\phi) \tag{21}$$

where $\lambda > 0$ and $\alpha \in \Re$ are the coefficients of the energy functions $\mathcal{L}_g(\phi)$ and $\mathcal{A}_g(\phi)$, which are defined as follows:

$$\mathcal{L}_g(\phi) \triangleq \int_\Omega g\delta(\phi)|\nabla \phi| dx \tag{22}$$

and

$$\mathcal{A}_g(\phi) \triangleq \int_\Omega gH(-\phi) dx \tag{23}$$

where δ and H are the Dirac delta function and the Heaviside function, respectively. Using the Dirac delta function δ, the energy $\mathcal{L}_g(\phi)$ computes the line integral of the function g along the zero level set contour of ϕ. By parametrizing the zero level set of ϕ\phi as $\mathcal{C}: [0,1] \to \Omega$, the energy $\mathcal{L}_g(\phi)$ can be expressed as the line integral

$\int_0^1 g(\mathcal{C}(s))|\mathcal{C}'(s)|ds$ This energy $\mathcal{L}_g(\phi)$ is minimized when the zero level set contour of ϕ coincides with the boundary of the target. It should be noted that the line integral $\int_0^1 g(\mathcal{C}(s))|\mathcal{C}'(s)|ds$ was originally introduced by Caselles et al. as the contour energy in their proposed GAC model. The energy function $\mathcal{A}_g(\phi)$ computes the weighted area of the region $\Omega_\phi^- \triangleq \{x: \phi(x) < 0\}$. For the specific case where $g = 1$, this energy exactly represents the area of the region Ω_ϕ^-. The energy $\mathcal{A}_g(\phi)$ is introduced to accelerate the motion of the zero level set contour during the evolution process of the level set, which is particularly necessary when the initial contour is far from the desired target boundary.

Here, the LSF is used such that negative values are inside the zero-level set contour and positive values are outside the zero-level set contour. In this case, if the initial contour is outside the target, the coefficient α in the weighted area should be positive so that the zero-level set contour can shrink during the evolution. If the initial contour is inside the target, the coefficient α\alpha should be negative to expand the contour. From the zero-level set evolution given in equation (27), it can be observed that the role of gg in the energy expression $\mathcal{A}_g$ is to slow down the shrinking or expanding of the zero-level set contour, and when it reaches the target boundary, g takes smaller values.

In practice, the Dirac delta function δ and the Heaviside function H in the functions $\mathcal{L}_g$ and $\mathcal{A}_g$ are approximated by smoothing functions $\delta_\mathcal{E}$ and $H_\mathcal{E}$ in many level set methods [18], defined as follows:

$$\delta_\mathcal{E}(x) = \begin{cases} \frac{1}{2\mathcal{E}}\left[1 + \cos\left(\frac{\pi x}{\mathcal{E}}\right)\right], & |x| \le \mathcal{E} \\ 0 & |x| > \mathcal{E} \end{cases} \tag{24}$$

and

$$H_\mathcal{E}(x) = \begin{cases} \frac{1}{2}\left(1 + \frac{x}{\mathcal{E}} + \frac{1}{\pi}\sin\left(\frac{\pi x}{\mathcal{E}}\right)\right), & |x| \ge \mathcal{E} \\ 1 & x > \mathcal{E} \\ 0 & x < -\mathcal{E} \end{cases} \tag{25}$$

Note that $\delta_\mathcal{E}$ is the derivative of $H_\mathcal{E}$, i.e., $H'_\mathcal{E} = \delta_\mathcal{E}$. The parameter EE is typically set to 1.5. The Dirac delta function δ and the Heaviside function H in equations (22) and (23) are replaced by $\delta_\mathcal{E}$ and $H_\mathcal{E}$, respectively, and the energy function $\mathcal{E}(\phi)$ is approximated as follows:

$$\mathcal{E}_\varepsilon(\phi) = \mu \int_\Omega p(|\nabla\phi|)dx + \lambda \int_\Omega g\delta_\varepsilon(\phi)|\nabla\phi|dx + \alpha \int_\Omega gH_\varepsilon(-\phi)dx \tag{26}$$

This energy function can be minimized by solving the following gradient flow:

$$\frac{\partial\phi}{\partial t} = \mu \mathrm{div}\big(d_p(|\nabla\phi|)\nabla\phi\big) + \lambda\delta_\varepsilon(\phi)\mathrm{div}\left(g\frac{\nabla\phi}{|\nabla\phi|}\right) + \alpha g\delta_\varepsilon(\phi) \tag{27}$$

The initial LSF$\phi(x, 0) = \phi_0(x)$, is specified. The first term on the right-hand side of equation (27) corresponds to the distance regularization energy $\mathcal{R}_p(\phi)$, while the second and third terms correspond to the energy terms $\mathcal{L}_g(\phi)$ and $\mathcal{A}_g(\phi)$, respectively. Equation (27) represents a geometric active contour model based on edges, which is an application of the general DRLSE formulation in equation (10).

2.3.2. Narrow Band Implementation

The computational cost of the level set method can be significantly reduced by limiting calculations to a narrow band around the zero level set. For the conventional level set formulation, implementing the narrow band requires repeated re-initialization or adding a speed expansion step. In the DRLSE formulation, there is no need for re-initialization or expansion speed in the narrow band implementation, due to the distance regularization effect during level set evolution. The narrow band implementation of DRLSE is simple and direct, such that the iteration process only involves updating the LSF according to the differential equation in equation (17) and generating the narrow band, as explained below. Additionally, the narrow band implementation of the DRLSE model in equation (27) allows the use of a large time step in the finite difference scheme to significantly reduce the number of iterations and computation time.

We define an LSF on a grid using $\phi_{i,j}$. A grid point (i,j) is referred to as a zero-crossing point, where $\phi_{i-1,j}$ and $\phi_{i+1,j}$ have opposite signs, or $\phi_{i,j-1}$ and $\phi_{i,j+1}$ have opposite signs. The set of all zero-crossing points of the LSF is denoted by Z. Then, we generate the narrow band.

$$B_r = \cup_{(i,j)\in Z} N_{i,j}^{(r)} \tag{28}$$

$N_{i,j}^{(r)}$ is a square block of size $(2r+1)\times(2r+1)$ centered at point (i,j). We can set r to its smallest value, r = 1, which represents the narrow band B_r, a union of 3×3 neighbors of the zero-crossing points. The narrow band implementation of DRLSE consists of the following steps:

1. **Initialization**: Initialize the LSFϕ with the function ϕ_0. Then, construct the initial narrow band: $B_r^0 = \cup_{(i,j)\in Z^0} N_{i,j}^{(r)}$ where Z^0 is the set of zero-crossing points of ϕ^0.
2. **Update LSF**: Update $\phi_{i,j}^{k+1} = \phi_{i,j}^{k} + \tau L(\phi_{i,j}^{k})$ within the narrow band B_r^k.
3. **Update Narrow Band**: Determine the set of all zero-crossing pixels $\phi_{i,j}^{k+1}$ in B_r^k, denoted by Z^{k+1}. Then, update the narrow band with: $B_r^{k+1} = \cup_{(i,j)\in Z^{k+1}} N_{i,j}^{(r)}$
4. **Assign Values to Pixels in the Narrow Band**: For each point (i,j) in B_r^{k+1} but not in B_r^k, if $\phi_{i,j}^{k+1} > 0$, set $\phi_{i,j}^{k+1}= h$, and otherwise set $\phi_{i,j}^{k+1}= -h$, where hh is a constant, typically set to r+1.
5. **Determine Termination of Iterations**: If the zero-crossing points change for mm consecutive iterations or exceed the maximum pre-set number of iterations, stop the iterations; otherwise, return to step 2.

The DRLSE not only eliminates the need for re-initialization but also allows the use of more general functions as the initial Level Set Function (LSF). The use of the binary step function as the initial LSF, as presented in equation (16), is suggested, as it can be effectively created. Moreover, the region R_0 in equation (16) can sometimes be obtained with an initial segmentation step, such as thresholding, so that R_0 closely approximates the segmented region. As a result, only a few iterations are required for the zero level set to move from the boundary of $R_0$to the desired target boundary.

As previously mentioned, the LSF using the binary step function is derived to approximate the signed distance function (SDF) around the zero level set. The width of the SDF is approximately $2c_0$. In practice, since the image domain is a discrete grid, the SDF should have at least one grid point on each side of the zero level set contour. Therefore, it is recommended to select c_0 from the range $c_0 \geq 1$. In this implementation, the value of c_0 is typically set to $c_0 = 2$, unless otherwise specified.

3. SIMULATION

3.1. Suitable Metric for Measuring the Accuracy of Medical Image Segmentation

As we know, after processing an image and performing segmentation, there is a need for an appropriate metric to compare the resulting image with the original one and quantitatively assess the segmentation accuracy. In this case, the commonly used metric, ρ, is employed for quantitative comparison. The ρ metric is calculated to compare the computed segmentation map SM with the ground truth segmentation map SM_{GT}.

$$\rho = 1 - \frac{\sum_{i=1}^{H}\sum_{j=1}^{W} \emptyset(Sm_{GT}(i,j), sm(i,j))}{HW} \tag{29}$$

where $\emptyset(a,b) = 1$ when a = b and $\emptyset(a,b) = 0$ when $a \neq b$. When Sm_{GT} and sm are identical, ρ equals "one," and ρ tends to zero as the dissimilarity between Sm_{GT} and sm increases. Therefore, a higher value of ρ indicates better segmentation.

3.2. Implementation Method and Images Used

All experiments in this study were implemented using MATLAB version 2013 on a Windows 7 operating system, executed on an HP laptop with a 7-core 4 GHz processor and 4 GB of internal memory. In this thesis, a simulated brain image was used. Since the regions in this image are precisely defined, we have the ideal segmented map. By adding noise to this image, we can create an image close to the real one with an accurate region map. The goal of using this image is to accurately calculate the segmentation algorithm's performance. Based on this accuracy, optimal parameter values for the algorithm can be determined by adjusting different algorithm parameters. To assess the algorithm's performance on real medical images, real images have been used, which consist of 3 different images with 256x256 pixel dimensions, with a corresponding ground truth segmentation map for each.

Considering the expansion of the number of directions in the filter bank created by the contourlet for feature extraction, it is beneficial to incorporate this property into feature extraction as well. These 8 features allow coverage of all eight extracted angles. In the contourlet transform, 8 features are extracted for each pixel, which results in an increase in the number of features. The number of features extracted is shown in Figure 2.

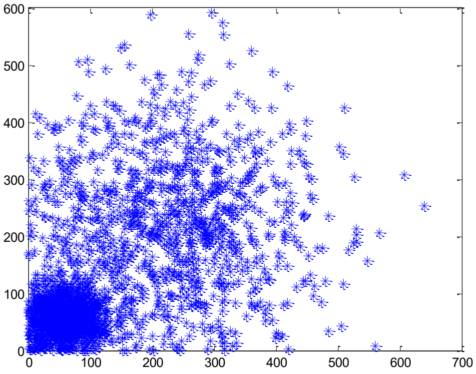

Fig. 1. Extracted features from the contourlet transform around the neighborhood of each pixel.

3.3. Adjustment of the Proposed Method

The configuration of the proposed algorithm consists of two main steps:

1. Adjustment of level set parameters (including the Gaussian kernel size (N) and its variance (sigma)
2. Adjustment of contourlet model parameters (including the number of iterations (N Iteration) and the coefficient (α))

Each of the following steps must be adjusted for each transformation. For example, the optimal number of iterations must be determined, or the level set adjustment should be examined. The evaluation criterion is the value of metric ρ, and parameters are chosen in each step in a way that maximizes this value.

3.3.1. Choosing the Number of Iterations for the Contourlet Model Algorithm

Here, the number of iterations should be evaluated. To do this, the number of iterations is varied from 20 to 230 in steps of 30. Experiments are conducted on the first image, and in each test, the value of metric ρ and the execution time are recorded. The objective is to select the highest ρ metric with the least execution time. The results obtained are shown in Table 1. Considering that there is little difference in the results between iteration numbers, and 8 subbands, but the execution time for 16 subbands is higher than for 8 subbands, the value of 8 subbands is chosen. Additionally, no significant difference is observed between the results at decomposition levels three and four, so decomposition level 3 is chosen.

Table 1. Results obtained for different decomposition levels and various subbands

Method	Iterations	α	Noise Variance Added to Image	Gaussian Kernel Size	Level Adjustment Variance	ρ
Contourlet+Levelset	20	1	32	1	0.01	-0.9524
Contourlet+Levelset	50	1	32	1	0.01	-0.4527
Contourlet+Levelset	80	1	32	1	0.01	0.0734
Contourlet+Levelset	110	1	32	1	0.01	0.5107
Contourlet+Levelset	140	1	32	1	0.01	0.8519
Contourlet+Levelset	170	1	32	1	0.01	0.9256
Contourlet+Levelset	200	1	32	1	0.01	0.9269
Contourlet+Levelset	230	1	32	1	0.01	0.9256
Contourlet	20	1	32	1	0.01	-0.7862
Contourlet	50	1	32	1	0.01	-0.0607
Contourlet	80	1	32	1	0.01	0.5536
Contourlet	110	1	32	1	0.01	0.8502
Contourlet	140	1	32	1	0.01	0.8572
Contourlet	170	1	32	1	0.01	0.8569
Contourlet	200	1	32	1	0.01	0.8572
Contourlet	230	1	32	1	0.01	0.8569

This table presents the results for different decomposition levels and various subbands using Contourlet and Contourlet+Levelset methods. The parameters considered include the number of iterations, the noise variance added to the image, Gaussian kernel size, level adjustment variance, and the correlation coefficient (ρ).

3.3.2. Selection of the α value for the Contourlet Model Algorithm

In this section, the number of iterations needs to be evaluated. To do this, the number of iterations is changed from 20 to 230 with steps of 30. The experiments are conducted on the first image, and for each experiment, the ρ criterion value and execution time are recorded. The goal is to select the maximum ρ value and the minimum execution time. The results obtained are shown in Table 2. Considering that there is little difference between the results for the number of iterations and 8, but the execution time for 16 subbands is longer than for 8 subbands, the value of 8 subbands is selected. Additionally, no significant difference is observed between the results at decomposition levels three and four, so decomposition level 3 is chosen.

Table 2. Results obtained for different decomposition levels and subbands values.

Method	Iterations	α	Noise Variance Added to Image	Gaussian Kernel Size	Level Adjustment Variance	ρ
Contourlet+Levelset	170	0.2	32	1	0.01	0.9142
Contourlet+Levelset	170	0.3	32	1	0.01	0.9135
Contourlet+Levelset	170	0.4	32	1	0.01	0.9139
Contourlet+Levelset	170	0.5	32	1	0.01	0.9125
Contourlet+Levelset	170	0.6	32	1	0.01	0.9149
Contourlet+Levelset	170	0.7	32	1	0.01	0.9139
Contourlet+Levelset	170	0.8	32	1	0.01	0.9119
Contourlet+Levelset	170	0.9	32	1	0.01	0.9125

This table presents the impact of different α values on the correlation coefficient (ρ) while keeping other parameters constant in the Contourlet+Levelset method.

3.4. Comparison of the Proposed Method with Other Methods

In this section, the proposed method is compared with other commonly used segmentation methods for brain MRI images. The proposed algorithm is compared with the active contour algorithm [7] and wavelet coefficient clustering [8]. The results obtained for three images are summarized in Table 3.

Table 3. Comparison of the results obtained for the proposed method with the active contour algorithm [1] and wavelet coefficient clustering algorithm [8] on three different images.

Method	Image No.	Execution Time (s)	ρ Metric (%)
Wavelet Coefficient Clustering [8]	1	2.15	97.93
Active Contour Method [7]	1	309	97.78
Proposed Method (Contourlet without Sampling)	2	19.78	93.50
Proposed Method (Contourlet with Sampling)	2	12.56	86.17
Wavelet Coefficient Clustering [8]	2	2.33	92.62
Active Contour Method [7]	2	288	88.06
Proposed Method (Contourlet without Sampling)	3	18.65	93.50
Proposed Method (Contourlet with Sampling)	3	12.45	91.98
Wavelet Coefficient Clustering [8]	3	2.22	92.25
Active Contour Method [7]	3	322	85.22

This table provides a comparison of execution time and ρ metric values for different image segmentation methods applied to three different images. The proposed method with Contourlet transformation demonstrates a trade-off between execution time and accuracy compared to existing approaches.

4. CONCLUSION

In this study, a segmentation algorithm titled "Brain Tumor Segmentation in MRI Images Using Transform Domain Methods" was proposed. The segmentation results obtained with different values of maximum decomposition levels and subband numbers demonstrate the relationship between preserving spatial details and reducing noise. Furthermore, the proposed algorithm performs almost identically for more than 8 subbands and decomposition levels greater than 3. The proposed DRLSE segmentation algorithm is computationally simple and yet effective in identifying meaningful regions in MRI images. Our experimental results show that the proposed algorithm is robust against noise in the datasets considered in this work, which makes it highly attractive for unsupervised brain tumor segmentation applications.

Using 8 subbands, as opposed to the common wavelet approach that only extracts coefficients in three directions, helps in identifying directional details of the image more effectively. Additionally, using 8 directional features for each pixel ensures that the extracted details across different subbands are reinforced based on similar directions, maximizing the use of subband correlations.

In a comparison between using the contourlet with sampling and contourlet without sampling, the sampling-free method proved to be significantly more successful. This success is likely due to the absence of downsampling and aliasing problems. It is also shift-invariant, meaning the energy decomposition of the image does not change across different decomposition levels. The final reason is that there is no need to rescale during the feature extraction process across various levels. In other words, while decomposing the image with sampling, we lose information, but for feature extraction, the coefficients need to be rescaled with higher-order coefficients, which also introduces unwanted noise, ultimately reducing the segmentation quality.

Transparency Statement

The data supporting this study are available upon reasonable request to the corresponding author, subject to ethical and confidentiality considerations.

Acknowledgments

We would like to express our gratitude to all individuals who contributed to this project.

Declaration of Interest

The authors declare that they have no competing interests.

Funding

This research received no specific grant from any funding agency, commercial, or not-for-profit sectors.

REFERENCES

[1] Razzak, M. I., Naz, S., & Zaib, A. (2017). Deep learning for medical image processing: Overview, challenges and future. ArXiv, abs/1704.06825. https://doi.org/10.1007/978-3-319-65981-7_12

[2] Shen, D., Wu, G., & Suk, H.-I. (2017). Deep learning in medical image analysis. Annual Review of Biomedical Engineering, 19, 221–248. https://doi.org/10.1146/annurev-bioeng-071516-044442

[3] Taha, A., & Hanbury, A. (2015). Metrics for evaluating 3D medical image segmentation: Analysis, selection, and tool. BMC Medical Imaging, 15. https://doi.org/10.1186/s12880-015-0068-x

[4] Zhou, Z., Siddiquee, M. R., Tajbakhsh, N., & Liang, J. (2018). UNet++: A nested U-Net architecture for medical image segmentation. Deep Learning in Medical Image Analysis and Multimodal Learning for Clinical Decision Support: 4th International Workshop, DLMIA 2018, and 8th International Workshop, ML-CDS 2018, held in conjunction with MICCAI 2018, Granada, Spain, S..., 11045, 3–11. https://doi.org/10.1007/978-3-030-00889-5_1

[5] Chartrand, G., Cheng, P., Vorontsov, E., Drozdzal, M., Turcotte, S., Pal, C., Kadoury, S., & Tang, A. (2017). Deep learning: A primer for radiologists. Radiographics: A Review Publication of the Radiological Society of North America, Inc., 37(7), 2113–2131. https://doi.org/10.1148/rg.2017170077

[6] Ker, J., Wang, L., Rao, J., & Lim, T. C. C. (2018). Deep learning applications in medical image analysis. IEEE Access, 6, 9375–9389. https://doi.org/10.1109/ACCESS.2017.2788044

[7] Gonzalez, R. C., Woods, R. E., & S. L. (2009). Digital image processing using MATLAB (2nd ed.). Gatesmark Publishing.

[8] Bankman, I. N. (2008). Handbook of medical image processing and analysis (2nd ed.). Academic Press.

[9] Peng, B., Zheng, L., & Yang, J. (2009). Iterated graph cuts for image segmentation. Asian Conference on Computer Vision (ACCV'09), Xi'an, China, 23–27.

[10] Niessen, W. J., et al. (2002). Multiscale segmentation of volumetric MR brain images. In Signal Processing for Magnetic Resonance Imaging and Spectroscopy (pp. 203–232). Marcel Dekker, Inc.

[11] Sonka, M., Hlavac, V., & Boyle, R. (2008). Image processing, analysis, and machine vision (3rd ed.). Thomson.

[12] Saha, S., Kumar, A., & Ekbal, A. (2016). Brain image segmentation using semi-supervised clustering. Expert Systems with Applications, 52, 50–63. https://doi.org/10.1016/j.eswa.2016.01.005

[13] Jiang, J., Wu, Y., Huang, M., Yang, W., Chen, W., & Feng, Q. (2013). 3D brain tumor segmentation in multimodal MR images based on learning population- and patient-specific feature sets. Computerized Medical Imaging and Graphics, 37(7–8), 512–521. https://doi.org/10.1016/j.compmedimag.2013.05.007

[14] Kanasa, V. G., Zacharakis, E. I., Davatzikos, C., Sgarbas, K. N., & Megalooikonomou, V. (2015). A low-cost approach for brain tumor segmentation based on intensity modeling and 3D random walker. Biomedical Signal Processing and Control, 22, 19–30. https://doi.org/10.1016/j.bspc.2015.06.004

[15] Li, C., Xu, C., Gui, C., & Fox, M. D. (2005). Level set evolution without re-initialization: A new variational formulation. Proceedings of the IEEE Conference on Computer Vision and Pattern Recognition, 1, 430–436. https://doi.org/10.1109/CVPR.2005.213

[16] Aubert, G., & Kornprobst, P. (2002). Mathematical problems in image processing: Partial differential equations and the calculus of variations. Springer-Verlag. https://doi.org/10.1007/b97428

[17] Evans, L. (1998). Partial differential equations. American Mathematical Society.

[18] Osher, S., & Fedkiw, R. (2002). Level set methods and dynamic implicit surfaces. Springer-Verlag. https://doi.org/10.1007/b98879